

# Lawrence Berkeley National Laboratory

## LBL Publications

### Title

On the Origin of Sinter-Resistance and Catalyst Accessibility in Raspberry-Colloid-Templated Catalyst Design

### Permalink

<https://escholarship.org/uc/item/3fs017bs>

### Journal

Advanced Functional Materials, 31(49)

### ISSN

1616-301X

### Authors

van der Hoeven, Jessi ES  
Krämer, Stephan  
Dussi, Simone  
[et al.](#)

### Publication Date

2021-12-01

### DOI

10.1002/adfm.202106876

Peer reviewed

# On the Origin of Sinter-Resistance and Catalyst Accessibility in Raspberry-Colloid-Templated Catalyst Design

Jessi E. S. van der Hoeven,\* Stephan Krämer, Simone Dussi, Tanya Shirman, Kyoo-Chul K. Park, Chris H. Rycroft, David C. Bell, Cynthia M. Friend, and Joanna Aizenberg\*

Nanoparticle (NP) sintering is a major cause of the deactivation of supported catalysts. Raspberry-Colloid-Templated (RCT) catalysts are an emerging class of materials that show an unprecedented level of sinter-resistance and exhibit high catalytic activity. Here a comprehensive study of the origin of NP stability and accessibility in RCT catalysts using theoretical modeling, 3D electron microscopy, and epitaxial overgrowth is reported. The approach is showcased for silica-based RCT catalysts containing dilute Pd-in-Au NPs previously used in hydrogenation and oxidation catalysis. Modeling of the contact line of the silica precursor infiltrating into the assembled raspberry colloids suggests that a large part of the particles must be embedded into silica, which is confirmed by quantitative visualization of >200 individual NPs by dual-axis electron tomography. The RCT catalysts have a unique structure in which all NPs reside at the pore wall but have >50% of their surface embedded in the matrix, giving rise to the strongly enhanced thermal and mechanical stability. Importantly, epitaxial overgrowth of Ag on the supported NPs reveals that not only the NP surface exposed to the pore but the embedded interface as well remained chemically accessible. This mechanistic understanding provides valuable guidance in the design of stable catalytic materials.

Preventing the growth of these small NPs into larger agglomerates, for example, at elevated temperatures and pressures, is challenging and remains a major cause of catalyst deactivation. Traditionally, high-surface-area supports are used to retard NP sintering by increasing the interparticle spacing.<sup>[2]</sup> Advances in material science have contributed to new routes to further increase the stability of NP catalysts.<sup>[3–11]</sup> Most prominent approaches are to distribute the particles in well-defined mesoporous supports,<sup>[2,12,13]</sup> to encapsulate the individual NPs in porous oxides,<sup>[4–7,14]</sup> to induce a thin metal oxide coating via strong metal-support interactions,<sup>[8,15]</sup> or by incorporating the NPs in a microporous framework, such as, for example, zeolites.<sup>[9]</sup> These designs drastically increase the thermal stability of the NPs and successfully protect the particles from sintering and Oswald ripening during catalysis.<sup>[3]</sup> However, the encapsulation can lead to a partial loss of catalytic activity


due to blockage of the NP surface by the surrounding metal oxide. A key challenge is to mitigate this effect, and to develop methodologies to probe the chemical accessibility of the NPs in these novel catalyst designs.

An emerging class of materials developed by our group that addresses this challenge is raspberry-colloid-templated catalysts (RCT).<sup>[16–24]</sup> The RCT materials exhibit exceptional thermal and catalytic stability,<sup>[17–21,23,24]</sup> while maintaining high

## 1. Introduction

Supported metal catalysts consisting of finely dispersed metal nanoparticles (NP) on high-surface-area supports are key in realizing cleaner and more efficient chemical conversions by lowering the energy cost and increasing the selectivity to the desired product.<sup>[1]</sup> Efficient use of precious metals is facilitated by dispersing the catalytically active metal in sub-10 nm parti-

J. E. S. van der Hoeven, C. M. Friend, J. Aizenberg  
Department of Chemistry and Chemical Biology  
Harvard University  
Cambridge, MA 02138, USA  
E-mail: jvanderhoeven@fas.harvard.edu; jaiz@seas.harvard.edu

 The ORCID identification number(s) for the author(s) of this article can be found under <https://doi.org/10.1002/adfm.202106876>.

© 2021 The Authors. Advanced Functional Materials published by Wiley-VCH GmbH. This is an open access article under the terms of the Creative Commons Attribution-NonCommercial-NoDerivs License, which permits use and distribution in any medium, provided the original work is properly cited, the use is non-commercial and no modifications or adaptations are made.

DOI: 10.1002/adfm.202106876

J. E. S. van der Hoeven, S. Dussi, T. Shirman, C. H. Rycroft, D. C. Bell, C. M. Friend, J. Aizenberg  
Harvard John A. Paulson School of Engineering and Applied Sciences  
Harvard University  
Cambridge, MA 02138, USA  
S. Krämer, D. C. Bell  
Center for Nanoscale Systems  
Harvard University  
Cambridge, MA 02138, USA  
K.-C. K. Park  
Department of Mechanical Engineering  
Northwestern University  
Evanston, IL 60208, USA  
C. H. Rycroft  
Computational Research Division  
Lawrence Berkeley Laboratory  
Berkeley, CA 94720, USA

catalytic activity<sup>[16–24]</sup> and selectivity.<sup>[17,20,21,24]</sup> The material design consists of an ordered macroporous metal oxide framework with sub 10-nm metal NPs distributed at the pore walls. The colloidal preparation approach that involves infiltration of the metal oxide precursor into the assembled sacrificial colloids decorated with catalytic NPs offers high versatility of the structural design, that is, particle size, metal composition, metal oxide composition, and micro- and macro-porosity can be tuned independently.<sup>[16,25]</sup> The robust, macroporous matrix allows facile mass transport throughout the catalyst.<sup>[26]</sup> The RCT approach therefore enables tailored design of oxidation<sup>[16–19,22,24]</sup> and hydrogenation<sup>[20,21,23]</sup> catalysts. So far, the potential of the RCTs for thermal catalysis has been demonstrated in selective alkyne hydrogenation,<sup>[20,21]</sup> HD exchange,<sup>[23]</sup> CO oxidation,<sup>[17,22]</sup> oxidative alcohol coupling,<sup>[17,24]</sup> and the oxidation of volatile organic compounds.<sup>[18]</sup> A unique feature of the RCT catalysts is their excellent stability during catalysis<sup>[18–20,24]</sup> and thermal treatment,<sup>[18,19]</sup> allowing long catalyst lifetimes and facile reactivation via thermal treatment.<sup>[21]</sup> A particularly noteworthy finding by Shirman et al. is the observation that not only the stability but also the activity of the RCT catalysts can be strongly enhanced compared to commercial catalysts, allowing drastic reductions in precious metal use and in energy cost in oxidation catalysis.<sup>[18]</sup>

The origin of the superior thermal stability of the RCT catalyst has remained an open question thus far. Furthermore, the crystal structure and accessibility of the catalytic NPs, in particular at their interface with the support, are still unknown despite the relevance of these properties to understanding the origin of sinter-resistance of these materials and their activity in catalysis. Here, by using theoretical modeling, 3D electron microscopy, and epitaxial overgrowth, we assess the NP embedding, the crystal structure, and the chemical accessibility of the metal NPs in RCT catalysts and discuss the implications of these structural characteristics for the catalysts' functional properties, and in particular for NP stability.

## 2. Results

### 2.1. Preparation of the Raspberry-Colloid-Templated Catalyst

The RCT preparation relies on multi-step synthetic route (Figure 1). The first step comprised the preparation of the metal NPs and amidine-functionalized polystyrene (PS) colloids ( $d = 307 \pm 10$  nm, Figure 1a). Here, the metal particles consisted of 96 atom % Au and 4 atom % of Pd, abbreviated as Au<sub>96</sub>Pd<sub>4</sub>, and were capped with polyvinylpyrrolidone (PVP). However, the desired composition, size, and shape of both the NPs as well as the size and functional surface groups of the PS colloids can be readily altered, independent of the subsequent synthesis steps, allowing a tailored design of catalysts for specific chemical reactions.<sup>[16]</sup> Next, the metal NPs were attached to the PS colloids, yielding so-called raspberry colloids (Figure 1b). An ordered colloidal crystal of raspberry colloids assembled by solvent evaporation (Figure 1c) was infiltrated with a pre-hydrolyzed silica sol-gel solution (Figure 1d). In the final step, the PS template and stabilizing ligands were removed via calcination (Figure 1e), generating an ordered macroporous silica support with metal NPs decorating the pore walls. Additionally, the high-tem-

perature calcination ensured the mixing of Pd and Au into a homogeneous alloy.<sup>[23]</sup> The resulting RCT catalyst contained  $\approx 5$  wt.% bimetallic Au<sub>96</sub>Pd<sub>4</sub> NPs as determined with inductively coupled plasma mass spectrometry (ICP-MS). The weight loading closely matches the theoretical weight loading of 4.8 wt.% calculated based on the synthesis parameters, indicating that no metal leaching occurred during the RCT preparation.

The sinter-resistance of the NPs in the RCT catalyst is evident from the overlapping size distributions before and after thermal treatment at 800 °C in static air (Figure 2). The average particle sizes before and after treatment closely match and are  $7.5 \pm 2.5$  and  $7.4 \pm 2.4$  nm, respectively. Additional long-term stability experiments show that thermally treating the catalyst for 10 h in either oxidizing or reducing gas atmospheres does not lead to particle growth (Figure S1, Supporting Information). These findings are in line with previous reports in which particle growth was not pronounced in RCT catalysts at temperatures up to 950 °C,<sup>[18]</sup> and in strong contrast to significant agglomeration and growth of NP in silica-supported catalysts in which the NPs were introduced after the macroporous silica framework was prepared.<sup>[19]</sup> Thermal treatment of the latter already led to particle growth to > 20 nm after thermal treatment at 500 °C in static air. In addition to the thermal stability of the NPs during synthesis and in oxidizing and reducing atmospheres, the long-term stability and sinter resistance of the PdAu and Pd NP RCT catalysts have been demonstrated for a range of reactions under catalytic conditions: CO oxidation,<sup>[19]</sup> methanol oxidation,<sup>[17]</sup> 1-hexyne hydrogenation,<sup>[20,21]</sup> and oxidation of simulated exhaust mixtures.<sup>[18]</sup> It has been shown that the sinter resistance is maintained in RCT catalysts even at high metal loadings and small NP sizes.<sup>[17–22,24]</sup>

### 2.2. Modeling the Geometry of the Nanoparticle-Silica Interfaces in RCT Catalysts Using Numerical Calculations

We postulated that the infiltration step in the synthesis procedure is crucial in determining the NP–silica interface and the degree of NP embedding into the matrix after calcination. More specifically, the geometry of the NP pocket within the silica support is defined by the wetting of the surfaces of the gold NPs and PS colloids by the infiltrating silica sol-gel solution. The wetting characteristics were assessed by measuring the equilibrium contact angles of the silica sol-gel on flat PVP-coated gold and amidine-functionalized PS substrates (Figure 1f). The pre-hydrolyzed silica sol-gel solution has a very low contact angle of  $\approx 10^\circ$  and  $30^\circ$  on a gold surface and PS surface, respectively. These contact angles and the sizes of the NPs and PS colloids (7.5 and 307 nm, respectively) were used as input for numerical calculations of the equilibrium solid-liquid-vapor contact line shapes that form a stable sol-gel interface between the NP and the PS colloid for different volumes of air trapped around NPs during the infiltration step (see Experimental Section for details). Specifically, the calculations allowed accessing the maximum possible air volume that gives a stable silica-air interface (Figure 1g). The upper limit is an air volume of  $\approx 1.6 \times 10^2$  nm<sup>3</sup>, yielding a minimum theoretical value for NP immersion into the sol-gel solution of at least 30% of its surface (i.e.,  $\approx 70\%$  exposure). Full NP immersion occurs when no air is trapped around the NP upon infiltration, and all the intermediate

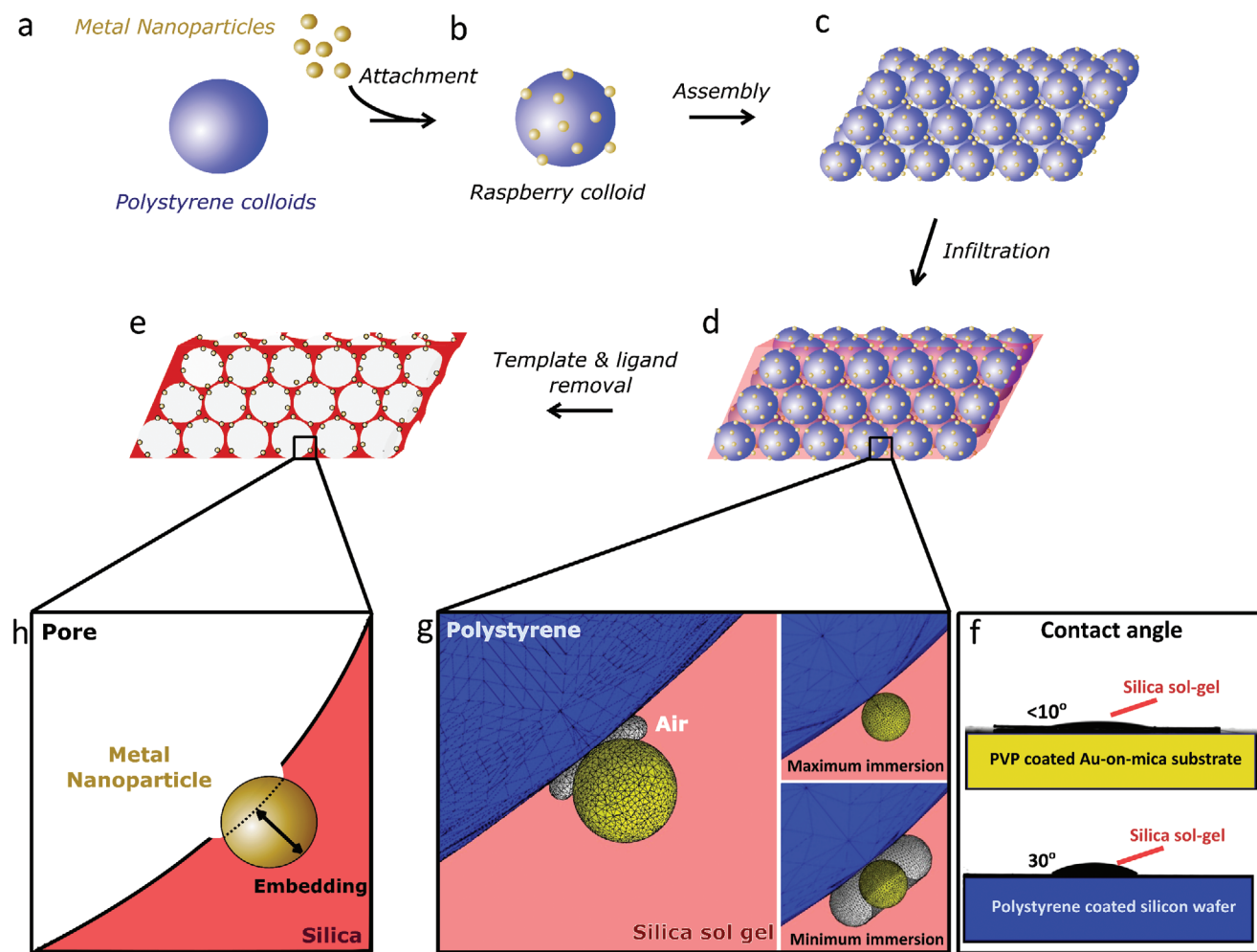


**Figure 1.** Effect of the infiltration step on the structure of RCT catalysts. a–e) Schematic of multi-step synthesis route: First, sacrificial PS colloids ( $d = 307 \pm 10$  nm) were decorated with gold-based NPs (a) creating so-called raspberry colloids (b). Subsequent self-assembly yielded a colloidal crystal (c), which was infiltrated with a silica sol-gel precursor (d). The PS colloids and the ligands around the metal NPs were removed via thermal treatment at  $500^\circ\text{C}$  in air (e), yielding an ordered macroporous silica support with the metal NPs residing at the pore-matrix interface. f) Measurement of the intrinsic, equilibrium contact angle that silica sol-gel mixture containing 33 vol% TEOS, 33 vol% ethanol and 33 vol% 0.1 M HCl in  $\text{H}_2\text{O}$  forms on a flat PVP-coated Au-on-mica substrate and a PS-coated silicon wafer. g) Snapshots of the numerical calculation results that show the equilibrium state silica sol-gel solution–air contact line at the particle–PS interface. The volume of the air bubble captured during infiltration affects the degree of NP immersion into the solution, where larger air bubbles lead to a lower degree of immersion. The snapshots on the right depict numerical calculations of two extreme cases: the largest captured air volume that can stabilize the contact line corresponds to the minimum possible value of 30% immersion of the NP into the solution (bottom) and full immersion takes place with no air trapped upon infiltration (top). h) Upon calcination, the immersed surface of the NPs will be embedded into the solidified silica matrix, suggesting that resulting RCT catalysts will comprise NPs residing at the pore interface with high embedding values of at least 30% of the NP surface.

immersion values are possible, as a function of the volume of air trapped around the individual NPs. Upon calcination, the immersed part of the particle will become embedded into the solidified silica matrix (Figure 1h), and hence, the NPs in the RCT catalysts are expected to be significantly entrenched, with a broad distribution of embedding values.

### 2.3. Quantifying the Nanoparticle Embedding Using Dual-Axis Electron Tomography

To verify the theoretical predictions, the embedding of more than 200 individual  $\text{Pd}_4\text{Au}_{96}$  NPs in silica-supported RCT catalyst

was quantified using dual-axis electron tomography (Figure 3). Previously, electron tomography has successfully been applied to obtain the distribution, size, and shape of metal particles in catalytic materials.<sup>[27–30]</sup> Yet, an important obstacle in using electron tomography to investigate metal-support interfaces is so-called missing wedge artifacts. These artifacts stem from the reduced range of orientations in which the sample can be imaged. Ideally, one would rotate the sample over the full  $180^\circ$  range, but in practice, only tilt angles in the range of  $140^\circ$  can be probed. The missing range of angles, called the missing wedge, causes artifacts in the final 3D reconstruction.<sup>[27,31,32]</sup> These artifacts are particularly severe around the metal particle due to diffraction contrast,<sup>[30]</sup> thereby obscuring the metal-support

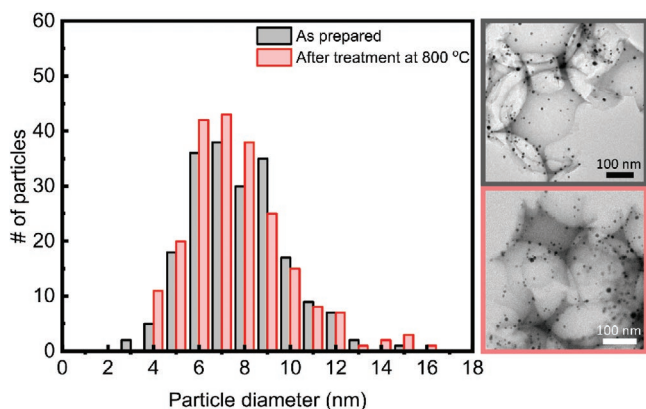


**Figure 2.** Thermal stability of silica-supported  $\text{Au}_{96}\text{Pd}_4$  RCT catalysts: no sintering at 800 °C. Size distributions before (black) and after thermal treatment at 800 °C (red), based on 200 particles per sample, and corresponding TEM images. The average particle size was  $7.5 \pm 2.5$  and  $7.4 \pm 2.4$  before and after thermal treatment, respectively. Conditions: static air, heating from room temperature to 800 °C at a rate of  $+5 \text{ °C min}^{-1}$ , followed by holding for 1 h at 800 °C.

interface and the local NP environment. Dual-axis tomography allows a significant reduction of missing wedge artifacts and therefore the assessment of the NP-support interfaces (Figure S2, Supporting Information).<sup>[31,33–35]</sup> As the direction of the artifacts around the metal particles depends on their orientation with respect to the tilt axis,<sup>[34,35]</sup> combining the information of two tilt series recorded over perpendicular axes, renders a more complete picture of the local NP environment.

The analysis procedure to achieve a quantitative and statistically relevant characterization of the local environment of the embedded NPs consisted of five steps (Figure S3, Supporting Information): i) acquisition and alignment of the tilt series, ii) separate reconstruction of both data sets, iii) recombination of the reconstructions, iv) segmentation into particle, support and pore, and v) quantification of the embedding. Full details are provided in the Experimental Section and Supporting Information. Both tilt series can be viewed in Movies S1 and S2, Supporting Information. No beam damage during the tomography acquisition occurred, which is crucial when combining the information from both tilt series into one (Figure S4, Supporting Information). Each series was individually processed by aligning the images using 12 fiducial markers in the 141 tilt images per data set and reconstructing the 2 tilt series separately (Figure S5, Supporting Information). Subsequently, the two 3D models were combined into one reconstruction using the known positions of 8 overlapping fiducial markers in both data sets (Movie S3, Supporting Information). The combined reconstruction at full resolution (0.385 nm per voxel size) consisted of more than  $3 \times 10^{10}$  voxels, making further analysis computationally challenging. Therefore, regions of interest (ROIs) of  $150 \times 150 \times 150$  voxels around the metal particles were carved out, allowing a reduction in the number of voxels by 3 orders of magnitude. To identify the ROIs, the images were downsized twice and a simple thresholding algorithm was applied to locate the NPs' positions. The coordinates obtained from the lower-resolution images were mapped back to the high-resolution images and the ROIs were extracted around

the estimated particles centers (Figure S6, Supporting Information). Successively, each ROI was segmented, that is, every voxel was classified as particle, support, or void (pore). The segmentation procedure consisted of i) denoising the raw images, by employing a total variation denoising algorithm; ii) identifying the voxels belonging to the particle, by applying contrast thresholding; iii) identifying the voxels belonging to the support, by employing a watershed algorithm (Figure S7, Supporting Information). From the segmented ROI, the particle size and the fraction of particle surface exposed to the pore were calculated. After visual inspection, accurate quantification of the local environment of 204 particles was confirmed (Figure S8, Supporting Information).

The quantitative analysis revealed that the NPs were indeed largely embedded in the silica support (Figure 3). The accuracy of our quantification procedure is supported by the excellent agreement between the average particle size as obtained via automatic segmentation (Figure 3b, top panel) and the manually measured particle size distribution based on a set of 2D images taken at different locations in the sample (Figure 2). Both approaches resulted in an average particle size of 7.4 nm. The relative amount of NPs surface area exposed to the macropores as a function of particle size for 204 particles present in the catalysts fragment, showed that 200 particles were more than 50% embedded in the support. The average and median exposed surface areas were 15% and 12%, respectively. However, the distribution of the exposed surface per particle in the right panel reveals that a substantial number of particles have less than 10% of the surface exposed. Furthermore, there are only 2 particles that have 60% of their surface exposed, which is the minimum embedding observed. As an example, two NPs, one moderately embedded (top, 36% surface exposed) and the other significantly embedded (bottom, 7% exposed), are shown in Figure 3c, where the green and yellow borders indicate the exposed and embedded NP surfaces, respectively. Overall, the distribution in exposed surface area is broad, and no obvious correlation between particle size and the amount of exposed NP surface was found. Both, the broad distribution of the particles exposed surfaces and the smallest observed embedding of 40% are in excellent agreement with the numerical modeling results shown in Figure 1g.

## 2.4. Penta-Twinned Particle Shape

The  $\text{Au}_{96}\text{Pd}_4$  NPs exhibited a characteristic penta-twinned crystal structure, irrespective of their size and degree of embedding (Figure 3d). Three representative particles of 9, 11, and 14 nm in diameter at different tilt angles are shown in Figure S9, Supporting Information. The diffraction contrast in the 2D images acquired at different tilt angles clearly shows the fivefold symmetry in the crystal structure of the particles. It is likely that this stems from the citrate ligands used in the NP synthesis, which are known to give rise to penta-twinned crystal structures in Au NPs.<sup>[36,37]</sup> The fivefold symmetry of the free-standing AuNPs remained intact after introducing a small amount of Pd, attaching the NPs to PS and thermally treating the RCT catalyst at 500 °C. This is in line with previous work in which the crystal structure of free-standing AuNPs was

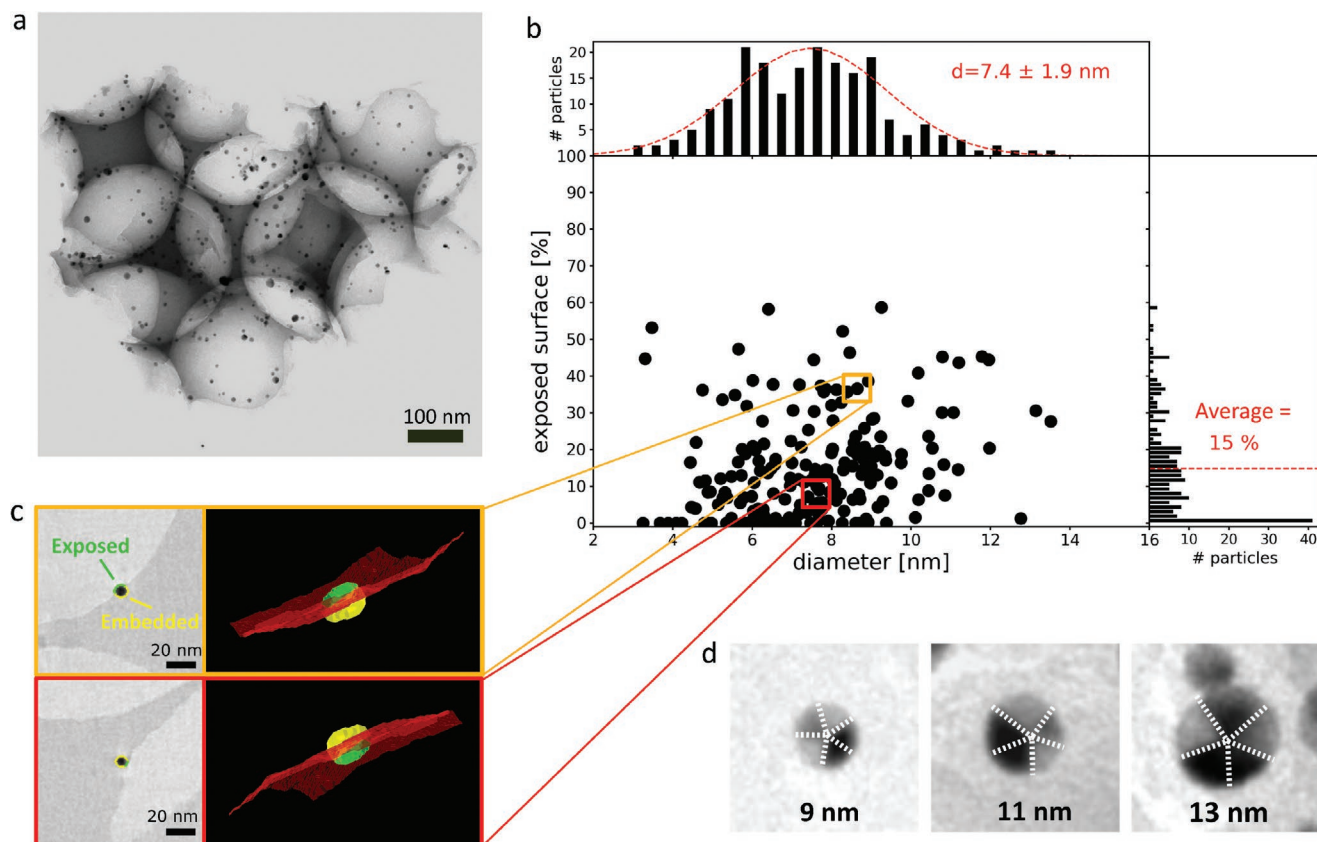


**Figure 3.** Electron tomography-based quantification of the exposed NP surface in  $\text{Au}_{96}\text{Pd}_4$  RCT catalyst. a) Bright field electron micrograph of the RCT catalyst containing  $\text{Au}_{96}\text{Pd}_4$  NPs on a silica support. b) Quantification of the exposed NP surface (%) as a function of particle size (nm) (middle panel), the particle size distribution (top panel), and the exposed surface distribution (right panel) for a total of 204 particles. The average particle size obtained from the tomography data analysis was  $7.4 \pm 1.9$  nm and the average particle surface exposed to the pore was 15%. c) Examples of 2 ROI containing an 8.4 nm particle with 36% surface exposed (top) and a 7.4 nm particle with 7% of the surface exposed (bottom). A 2D slice of the analyzed 3D region is shown, with the green and yellow border indicating the exposed and embedded NP surface, respectively. A set of 2D slices of the particle with 36% surface exposed is shown in Figure S4, Supporting Information. d) Representative  $\text{Au}_{96}\text{Pd}_4$  NPs with a diameter of 9, 11, and 14 nm showing the penta-twinned crystal structure. Additional 2D projection images recorded at different tilt angles are shown in Figure S9, Supporting Information.

studied as a function of temperature.<sup>[38]</sup> The decahedral shape of 2–10 nm AuNPs was stable up to 550–600 °C, above which surface roughening and ultimately melting occurred. Another indication that the penta-twinned crystal structure was preserved during the RCT synthesis, is the random orientation of the facets with respect to the pore, which is expected, based on the random attachment of the metal NPs to the PS colloids. No evidence for differences in faceting of the exposed and embedded side of NPs was found.

### 2.5. Epitaxial Overgrowth for Direct Visualization of the Nanoparticle Accessibility

The electron tomography data provided quantitative information on the embedding of the metal NPs in the silica matrix and insight into the particle shape, but raised the question of whether the heavily embedded interfaces of the NPs were still chemically accessible. To assess this, a novel and complementary characterization approach was employed, relying on epitaxial overgrowth of the embedded NPs with a second metal, in this case, silver. Ag was chosen as it is known to grow

epitaxially on Au due to the negligible lattice mismatch between the two metals ( $d_{\text{Au-lattice}} = 407.82$  pm,  $d_{\text{Ag-lattice}} = 408.53$  pm).<sup>[39]</sup> Hence, the epitaxial growth of Ag on Au enabled visualization of the crystal orientation of the Au surface facets exposed to the macropores. Furthermore, Ag has a significantly lower Z-contrast compared to Au, ensuring a clear difference between the Ag-shell and AuNPs in the electron microscopy visualization.

The Ag-shell growth on free-standing and embedded AuNPs is distinctly different (Figure 4). The high-resolution high-angle annular dark-field scanning transmission electron microscopy (HAADF-STEM) image (Figure 4a–c) shows a smooth, epitaxial spherical Ag-shell around the free-standing AuNPs with roughly the same 1.5 nm shell thickness at all sides, whereas clear anisotropic Ag-shell growth was observed on the embedded AuNPs (Figure 4d–f). The difference in Ag-shell morphology is also evident from the UV–vis spectra (Figure 4c,f). The localized surface plasmon resonance (LSPR) of the free-standing AuNPs blue-shifted from 517 to 500 nm and increased in intensity upon Ag growth, which is in line with previously reported theoretical and experimental work, where the increase in intensity of the LSPR peak can be ascribed to both the stronger plasmonic properties of Ag and

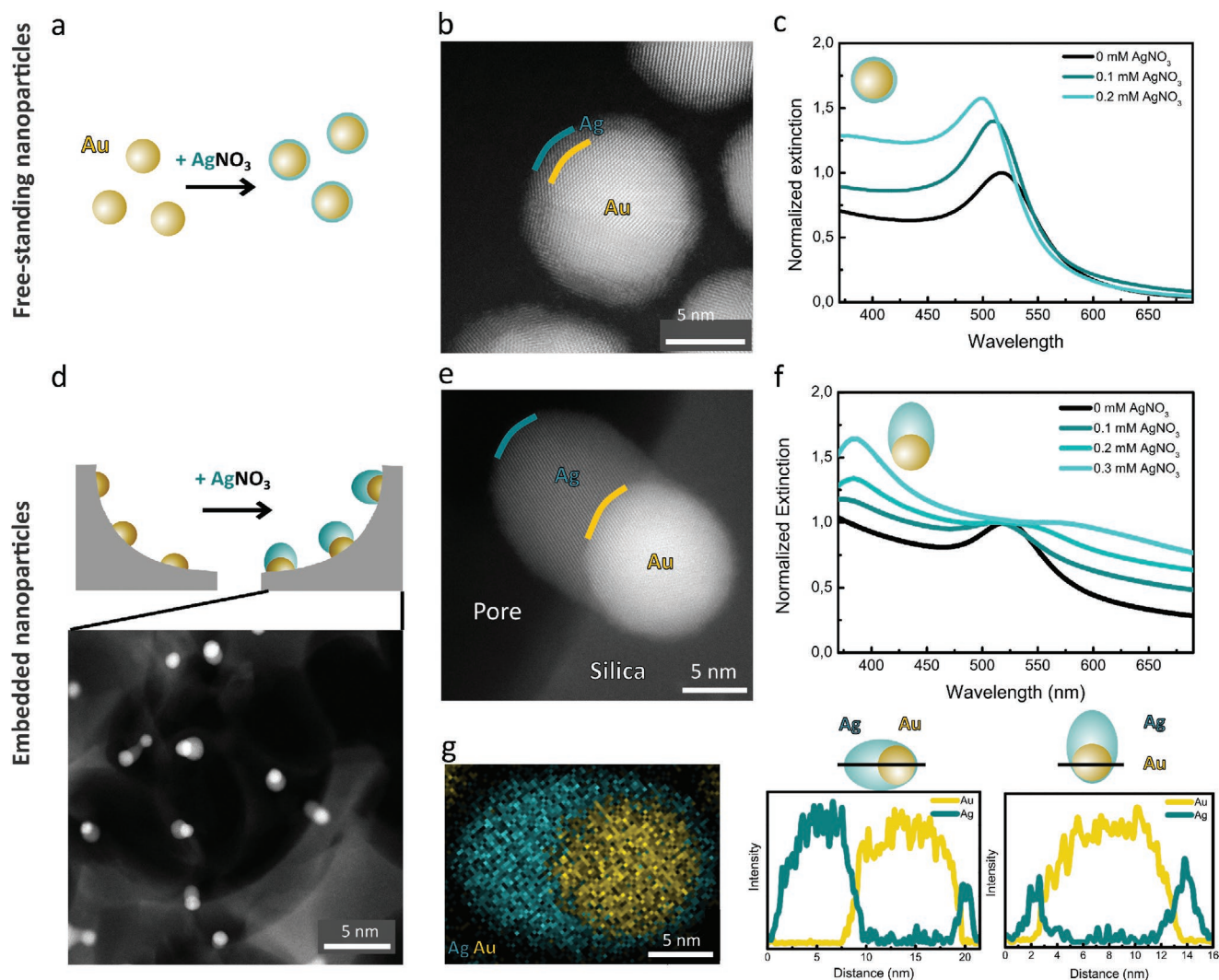


**Figure 4.** Probing the chemical accessibility of metal particles using silver overgrowth. (a–c) Ag overgrowth on free-standing gold NPs (AuNPs): a) Schematic. b) Corresponding HAADF-STEM image showing isotropic Ag-shell growth around the Au-core. c) UV–vis spectra showing a blue shift in the LSPR upon Ag-shell growth around free-standing AuNPs. (d–g) Ag overgrowth on AuNPs embedded in the silica matrix within RCT catalysts: d) Schematic. e) Corresponding HAADF-STEM image showing anisotropic Ag-shell growth, resulting in Janus-like NPs. The Ag-shell is single-crystalline with a lattice spacing of 0.235 nm, corresponding to the {111} facet. f) UV–vis spectra showing that the LSPR peak splits up in a transverse and longitudinal LSPR mode at high and low energy, respectively, indicating anisotropic Ag-shell growth. g) EDX Analysis displaying the Ag-shell and Au core in blue and yellow, respectively. The plots show the intensity of the Au and Ag signal along the length and width of the Janus particle, and reveal that also a thin Ag-shell was present along the embedded side of the AuNPs.

increase in particle volume.<sup>[39]</sup> Contrarily, the LSPR peak of the embedded AuNPs split up into 2 separate peaks upon Ag-shell growth: a transverse and longitudinal LSPR peak, at high and low energy, respectively, similar to the plasmonic properties of Ag nanorods.<sup>[40]</sup> The red-shift of the longitudinal LSPR peak from 521 to 565 nm indicates the growth of a more elongated particle, and hence matches well with the particle Janus-like shape observed in the HAADF-STEM images. In both cases, the shell thickness was controlled via the AgNO<sub>3</sub> concentration in the reaction mixture.

Although the Ag-shell preferentially grew on the NP surface exposed to the macropores, Energy-dispersive X-ray spectroscopy (EDX) analysis revealed that Ag also grew on the embedded side of the NPs. This is further confirmed by the high-resolution

images in **Figure 5**, where a continuous shell of approximately three atomic Ag layers was observed on the embedded side of the NPs ( $d_{\text{Ag-shell}} = 0.7$  nm). Furthermore, the crystal structure of the Ag-shell provided insight into the type and number of surface facets of the AuNPs facing the macropores. By “freezing in” the surface structure of the NPs in the Ag-shell, imaging at high resolution was possible without beam-induced restructuring. The high-resolution images in Figure 5 reveal that depending on the type of facets exposed to the pore, either single-crystalline or twinned Ag-shell formed. In line with our findings shown in Figure 4, no evidence for preferential orientation of specific surface facets towards the macropores was observed.

The embedded metal surface area could be available to the reactants through the 0.7 nm gap, but its accessibility

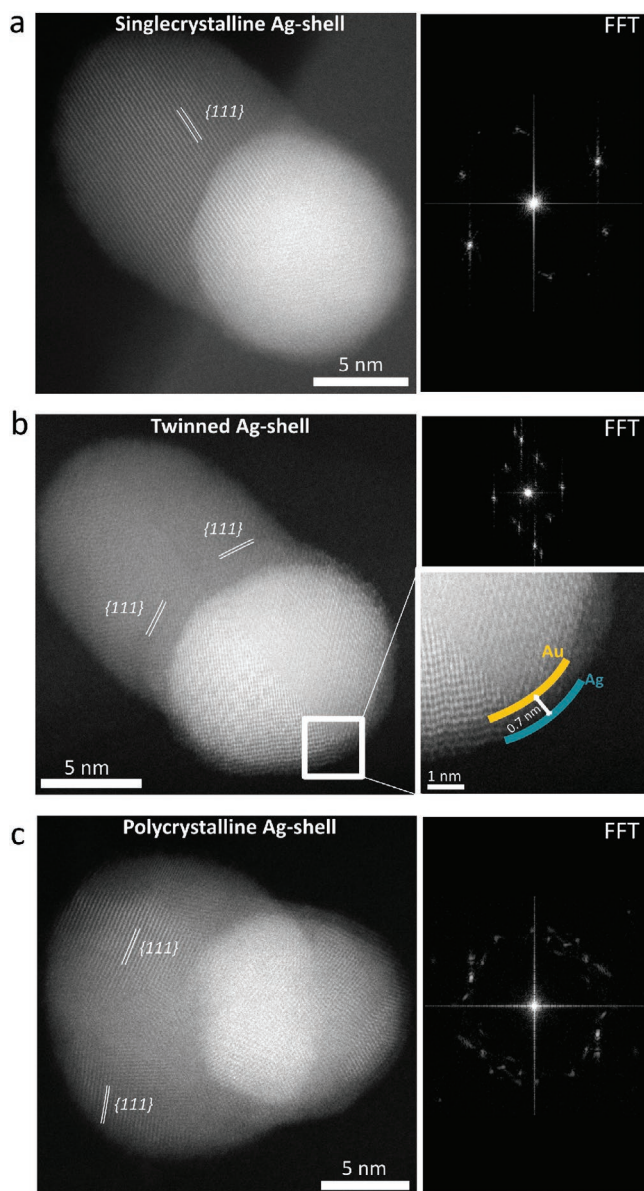


**Figure 5.** Visualizing the crystal structure of the exposed NP facets—HAADF-STEM images and corresponding Fast Fourier Transform (FFT) of a) poly-crystalline, b) single-crystalline, and c) twinned Ag shell. The inset in b shows a 0.7 nm thin Ag shell on the embedded side of the AuNPs.

might also be related to the porosity of the silica support itself. As the micropores cannot easily be characterized using electron microscopy, nitrogen physisorption was employed to investigate the effect of the latter. The physisorption data (Figure S10, Table S1, Supporting Information) confirm that the silica support is indeed microporous ( $V_{\text{micro}} = 0.073 \text{ cm}^3 \text{ g}^{-1}$ ), thereby allowing mass-transport to the embedded part of the AuNPs. Furthermore, the physisorption data show that the porosity of the matrix can be tuned via thermal treatment, where repetitive thermal treatment at elevated temperature reduces the microporosity of the silica matrix.

### 3. Discussion

The numerical calculation, tomography, and overgrowth results concur in showing that the NPs in RCT catalysts are substantially embedded in the silica support. 200 out of 204 particles were more than 50% embedded in the silica support, and the majority of particles even more than 90%. NP embedding is known to prevent both Oswald ripening and particle sintering, the two mechanisms for particle growth.<sup>[3,41]</sup> The large degree of embedding, and in particular the fact that the particles are embedded up to or above their waste line, prevents particle dislodgement and migration, explaining the absence of NP growth even upon thermal treatment at 800 (Figure 2) and 950 °C,<sup>[18]</sup> and during catalysis at elevated temperatures.<sup>[17–21,24]</sup> The thermal stability is substantially enhanced compared to gold-based catalysts with NPs lying on top of the support surface, which start to grow to larger particle sizes below 800 °C,<sup>[12,19,42]</sup> and is comparable to fully encapsulated NPs.<sup>[5,6]</sup> Hence, the RCT preparation approach endows a robust, porous 3D architecture with all catalytic NPs residing on the pore surfaces and available to the reactants, but significantly embedded into and thus stabilized within the support. The macropores ensure facile mass transport throughout the catalysts, preventing mass-transport limitations in the catalyst bed, whereas the micropores of the matrix enable local diffusion to the embedded side of the NP surface. An additional advantage of the RCT methodology over direct encapsulation in porous shells is the possibility for facile tuning of the composition of the supporting oxide, for example, to a mixed titania-silica,<sup>[25]</sup> titania,<sup>[16,25]</sup> alumina,<sup>[16,18]</sup> and zirconia<sup>[16]</sup> support, and therefore control over the metal-support interactions.

The high degree of embedding originates from the preparation method, in particular from the infiltration stage when favorable wetting of the PS colloids and gold particles by the silica sol-gel solution necessitates the formation of the equilibrium solid-liquid-vapor contact line at high immersion values of the NPs into the silica precursor, as confirmed by the contact angle measurements and numerical modeling in Figure 1f,g. The favorable wetting stems from the high ethanol content (33 vol%) in the silica sol-gel, which significantly lowers the surface tension of the sol-gel. As a result, the NPs are close to fully wetted irrespective of their size. The large spread in NP embedding (Figure 3b) likely originates from the varying volume of air that can be trapped around the NPs during infiltration. Indeed, the numerical calculations of the equilibrium contact line (Figure 1f) show that exposed surface area can vary between 0 and 70% depending on the volume of the air trapped around the NPs. This is in line with the quantitative analysis in Figure 3b, where the exposed surface areas of all 204 particles lie between 0 to 60% exposed surface area. Future work can be directed to tune the degree of embedding via the composition of the sol-gel precursor and via the NP surface functionalization, allowing structural control over the metal-support interface geometry.

The embedding in the support did not affect the NP morphology. The crystal structure of the NPs in the RCT catalysts was penta-twinned which matches that of free-standing Au NPs.<sup>[36–38]</sup> Furthermore, the orientation of their facets was random with respect to the pore, which is consistent with the random attachment of the NPs to PS colloids during the



raspberry colloid preparation (Figure 1b).<sup>[16]</sup> The absence of asymmetries in the particle structure due to the embedding is expected given that the silica support is porous (Figure S10, Table S1, Supporting Information), meaning that both the embedded and exposed particle sides are subjected to the same type of gas atmosphere upon treatment. Finally, we want to note that identifying the 3D shape for small NPs (5–10 nm) is not trivial as restructuring during electron beam illumination can occur.<sup>[43]</sup> This was avoided in this work by recording the data set at a relatively low magnification (29k $\times$ ), thereby decreasing the electron dose and increasing the number of NPs in the field of view.

The epitaxial overgrowth experiments show that both the exposed as well as the embedded side of the NPs are chemically accessible. The chemical accessibility of the embedded NP surface is likely due to mass transport through the micropores of the silica support. Additionally, the chemical accessibility could be explained by a small gap between the embedded surface and silica support resulting in the observed 2–3 atom thick Ag shell growth. Whether and how the embedded side contributes to the catalytic performance is an open question. Yet, it is worth mentioning that the embedding doesn't necessarily lead to reduced reactivity compared to non-embedded NP catalysts. In fact, Shirman et al. showed that Pd on alumina RCT catalysts were significantly more active compared to the traditionally supported catalysts, allowing a 90% reduction of the Pd loading compared to the conventional catalysts with the same catalytic performance.<sup>[18]</sup> Hence, the contribution of the embedded interfaces, that is, their chemical structure and accessibility, should be carefully considered in interpreting the reactivity of these materials. Likely, the contribution of the embedded NP surfaces to the catalytic performance is an interplay between mass-transport limitations and nano-confinement effects. B. Dong et al. demonstrated that mass-transport to embedded NP surfaces is suppressed, but that the catalytic activity at the embedded surface itself is significantly increased due to nano-confinement effects.<sup>[44]</sup> Such nano-confinement effects<sup>[44,45]</sup> can arise due to local enhancement of the reactant concentrations, altered adsorption-desorption equilibria, and/or stabilization of reactant intermediate species or states,<sup>[44]</sup> yielding enhanced catalytic activity and potentially altered product selectivity.

Our combined tomography and epitaxial overgrowth approach is not limited to the RCT catalysts studied here, but can be extended to catalytic and nanostructured materials in general. Visualization of metal-support interfaces in 3D materials using only 2D imaging techniques can give deceiving information as the imaging orientation influences the appearance of the metal-support interfaces, which is why electron tomography is preferred, even for qualitative studies. Important parameters to consider in applying tomography are the Z-contrast between the individual components and the stability of the sample under electron beam illumination. Ideally, the difference between the metal, support, and pores of the catalyst is large, allowing facile segmentation. Alternatively, the metal overgrowth approach is simpler and quicker compared to electron tomography, allowing the direct assessment of the NP accessibility and a qualitative understanding of the metal-support geometry. The metal overgrowth methodology can easily be adapted to match a specific catalyst system by choosing a

suitable metal for the overgrowth. Herein, the most important considerations are the difference in Z-contrast between the core and shell, and the growth behavior of the metal shell. The choice of metal is critical in ensuring epitaxial growth and a well-defined shell morphology. Epitaxial shell growth is achieved by choosing a metal with a lattice constant closely matching the underlying core ( $\leq 5\%$ ).<sup>[46]</sup> Smooth and continuous shell growth is ensured by a favorable interaction between the core and the shell, meaning that the second metal preferentially deposits on the cores.<sup>[46]</sup> Furthermore, sufficiently slow overgrowth kinetics are important to ensure homogeneous shell growth throughout the sample, which can be achieved by using mild reducing agents, and by controlling the growth rate via, for example, pH and reaction temperature.<sup>[39]</sup>

## 4. Conclusion

The sinter-resistance of RCT catalysts finds its origin in the large degree of NP embedding in the supporting oxide. A combined approach of numerical modeling, tomography, and epitaxial overgrowth provided quantitative insight into the mechanistic underpinnings of such a unique geometry of the metal-support interfaces, as well as morphology and accessibility of hundreds of metal NPs in the RCT catalyst design, and showed that although the NPs were significantly embedded, their entire surface remained chemically accessible. Our results unequivocally show that the key to the substantial NP embedding is the favorable particle wetting by the silica sol-gel during the infiltration step in the synthesis. Hence, the potential of the RCT material design lies in the ability to tune the metal-support interface geometry via the wetting behavior of the metal oxide precursor, and the control over the resulting NP stability and accessibility.

## 5. Experimental Section

**Chemicals:** All chemicals were used as received without further purification. Hydrogen tetrachloroaurate trihydrate ( $\text{HAuCl}_4 \cdot 3\text{H}_2\text{O}$ ,  $\geq 99.9\%$ ), sodium borohydride ( $\text{NaBH}_4$ , 99%), palladium nitrate ( $\text{Pd}(\text{NO}_3)_2$ ,  $\geq 99.9\%$ ), silver nitrate ( $\text{AgNO}_3$ ,  $\geq 99\%$ ), sodium citrate tribasic dihydrate ( $\geq 99.0\%$ ), potassium carbonate ( $\text{K}_2\text{CO}_3$ ,  $\geq 99.0\%$ ), tannic acid, L-ascorbic acid ( $\geq 99.0\%$ ), PVP (MW  $\approx 55\,000\text{ g mol}^{-1}$ ), styrene (contains 4-tert-butylcatechol as stabilizer,  $\geq 99\%$ ), 2,2'-Azobis(2-methylpropionamide) dihydrochloride (AAPH, 97%), and tetraethyl orthosilicate (TEOS, 98%) were purchased from Sigma-Aldrich. Absolute ethanol (EtOH) was purchased from KOPTEC. Ultrapure water (Millipore Milli-Q grade) with a resistivity of 18.2 M $\Omega$  was used in all of the experiments. All glassware for the AuNP synthesis was cleaned with fresh aqua regia ( $\text{HCl}/\text{HNO}_3$  in a 3:1 volume ratio), rinsed with large amounts of water, and dried at 130 °C before usage.

**Catalyst Synthesis:** The catalyst preparation relies on a colloidal, multistep synthesis procedure.<sup>[16]</sup> Below all synthesis steps are outlined in detail.

**Gold Nanoparticles:** For the AuNP used to prepare the  $\text{Au}_{96}\text{Pd}_4@$   $\text{SiO}_2$  catalysts, the procedure of Grabar et al. was followed.<sup>[47]</sup> Briefly, 200 mL MilliQ water and 1.0 mL aqueous 70 mM  $\text{HAuCl}_4$  solution were mixed in a 500 mL round bottom flask. After  $\approx 10$  min of stirring at room temperature, 1.0 mL aqueous 170 mM sodium citrate pre-mixed with 100  $\mu\text{L}$  of an ice-cold aqueous 240 mM  $\text{NaBH}_4$  solution was added while stirring vigorously. The color of the reaction mixture changed rapidly

from yellow to dark purple. The flask containing reaction mixture was wrapped in aluminum foil and left under moderate stirring overnight, during which the color of the reaction mixture changed from purple to red. Finally, the larger particles were removed by centrifugation (9500 rpm  $\times$  45 min). For the 11 nm AuNPs used for the Ag overgrowth, the procedure described by Piella et al was followed.<sup>[48]</sup> Briefly, 150 mL 2.2 mM trisodium citrate in MilliQ water was added to an aqua-regia-clean 250 mL two-neck round bottom flask connected to a (ice-)water-cooled reflux condenser. The reaction mixture was heated to 70 °C in an oil bath, while stirring magnetically at 400 rpm (revolutions per minute). Next, 0.10 mL 2.5 mM tannic acid and 1.0 mL 150 mM K<sub>2</sub>CO<sub>3</sub> were added while increasing the stirring speed to 700 rpm. Thereafter, 1.0 mL 25 mM HAuCl<sub>4</sub> in H<sub>2</sub>O was added. The reaction mixture turned yellow to gray and a few minutes later to orange-red. After 10 min, 55 mL of the reaction mixture was removed and 55 mL 2.2 mM sodium citrate solution was added. Next, 0.50 mL 25 mM HAuCl<sub>4</sub> solution was added twice at a 10 min time interval. Thereafter, 55 mL of the reaction mixture was removed and 55 mL 2.2 mM sodium citrate solution was added, followed by the addition of HAuCl<sub>4</sub>. This step was done 4 times in total to arrive at an 11 nm large AuNPs.

**Pd Overgrowth:** The Pd overgrowth on the AuNPs was carried at room temperature in water. First, 250 mL of as-synthesized citrate stabilized AuNPs solution was mixed with 5.0 mL of an aqueous 2.5 M ascorbic acid solution under stirring ( $\approx$ 400 rpm). For the Au<sub>96</sub>Pd<sub>4</sub> NPs, 270  $\mu$ L of an aqueous 15.8 mM Pd(NO<sub>3</sub>)<sub>2</sub> solution was added stepwise ( $\approx$ 70  $\mu$ L per 30 min). The reaction mixture was stirred for  $\approx$ 12 h at room temperature.

Next, 1.0 g of PVP (MW = 55 000 g mol<sup>-1</sup>) dissolved in 10 mL of MQ water was added and stirred for an additional 30 min. Finally, the larger particles were removed by centrifugation (9500 rpm  $\times$  35 min).

**Polystyrene Colloids:** The PS colloid synthesis was carried out in a 500 mL three-necked round bottom flask, to which a reflux condenser, thermometer connected to a heating mantle, and septum with a syringe needle were mounted. 178 mL of MQ H<sub>2</sub>O was added, which was degassed by bubbling nitrogen through it for at least 30 min, while being heated to 65 °C. After the temperature of the water had stabilized, 20 mL of styrene was added, while stirring at 300 rpm and degassing with nitrogen. After 5 min, 2.0 mL of 0.10 g mL<sup>-1</sup> AAPH in H<sub>2</sub>O was added. The degassing continued for another 30 min. Thereafter, the mixture was refluxed at 65 °C for 12 h. Next, the solution was transferred into dialysis tubes and cleaned by changing the water twice a day for 1 week.

**Raspberry Colloids:** The raspberry colloids were prepared by attaching the metal particles to the PS colloids. For the Au<sub>96</sub>Pd<sub>4</sub> NPs, 110 mL NPs were attached to 10 mL PS colloid dispersion ( $d_{PS}$  = 420 nm, 5.5 wt.% in water) by slow drop-wise addition of the NPs to the PS colloid dispersion under continuous stirring at 400 rpm. Next, the raspberry colloids were washed 3 times with MQ H<sub>2</sub>O (centrifugation: 9500 rpm  $\times$  30 min) and re-dispersed in 11 mL MQ H<sub>2</sub>O (5.0 wt.% PS in water). For the 11 nm AuNPs, 50 mL NPs were added to 6.1 mL PS colloid dispersion ( $d_{PS}$  = 307 nm, 9.5 wt.% in water). Next, 2  $\times$  100  $\times$  diluted HNO<sub>3</sub> in H<sub>2</sub>O were added to lower the pH to 4. The resulting raspberry colloids were washed 3 times with H<sub>2</sub>O (centrifugation: 9500 rpm  $\times$  45 min) and re-dispersed in 12.5 mL MQ H<sub>2</sub>O (5.0 wt.% PS in water).

**RCT Preparation:** The 3  $\times$  5 mL raspberry colloid dispersion (5.0 wt.% PS in water) was dried in 3 separate vials at 65 °C in air. To each vial  $\approx$ 200  $\mu$ L of prehydrolyzed TEOS solution (33 vol% of a 0.10 M HCl in H<sub>2</sub>O solution, 33 vol% ethanol, 33 vol% TEOS) was added to infiltrate the dried colloidal crystal. Thereafter the sample was dried again at 65 °C. This step was repeated 3 times. The samples were calcined by heating them in static air from room temperature to 500 °C with 1.9 °C min<sup>-1</sup> and held at 500 °C for 2 h, and then cooled to room temperature over 3–4 h. The final particle size for the Au<sub>96</sub>Pd<sub>4</sub>@SiO<sub>2</sub> and Au@SiO<sub>2</sub> catalysts was 7.6  $\pm$  2.3 and 11  $\pm$  2.0 nm.

**Ag Overgrowth:** The Ag overgrowth was performed on the Au(11 nm)@SiO<sub>2</sub> sample. 7.2 mg sample was dispersed in 7.20 mL MQ H<sub>2</sub>O via sonication. To 1.0 mL dispersion, 10  $\mu$ L 0.10 M HCl and equal amounts (5, 10, 20, or 30  $\mu$ L) of 10 mM AgNO<sub>3</sub> and 40 mM ascorbic acid in H<sub>2</sub>O were added, while shaking vigorously (method adapted from ref. [39]). The mixture was left to react for 30 min. Thereafter, the UV–vis

spectra shown in Figure 5 were recorded. The samples were washed once with 1 mL H<sub>2</sub>O (centrifugation: 9500 rpm  $\times$  10 min), re-dispersed in 200  $\mu$ L ethanol, and stored in the fridge at 4 °C to prevent oxidation and dissolution of the Ag-shell.

**Electron Microscopy:** Electron microscopy was used for structural analysis. The samples were dispersed in absolute ethanol and drop-casted onto a Formvar/Carbon 200 mesh copper grid (TedPella). The HAADF-STEM was carried out on a JEOL ARM 200F STEM equipped with a cold field emission gun (FEG, operated at 200 keV) and integrated aberration corrector (Cs). The bright-field TEM tomography measurements were performed on a F20 Tecnai (Thermo Fisher) operated at 200 kV and a 2k  $\times$  2k UltraScan CCD camera (Gatan).

Prior to the tomography measurement, fiducial markers were deposited using a Helios Nanolab 660 Focused Ion Beam microscope (Thermo Fisher). After carefully selecting a sample fragment that has the proper size for the desired tomographic parameters, a 9  $\times$  9 array of Pt cones was centered around the particle with a total dimension of 80% of the CCD viewing field at the given magnification. Applying a 30 kV voltage beam with a 0.1 nA current, a 160  $\mu$ s exposure of a circle with a 1 nm diameter produced cylindrical cones with an approximate diameter of 30 nm and a height of 90 nm. For the process, TEM samples were placed in a STEM holder orienting the samples identical to the final position in the TEM tilt holder; an insertable STEM detector was used for sample survey and selection of the proper region of interest. Short exposure times ensured sufficient suppression of carbon contamination during scans. The pre-defined position and highly reproducible shape of the cones allowed easy tracking of the fiducial markers. Furthermore, the vast majority of the actual sample area was unobstructed by objects as it would typically be the case for randomly positioned, pre-deposited gold particles.

The dual-axis tilt series were recorded using SerialEM on a F20 Tecnai (Thermo Fisher) operated at 200 kV equipped with a 2k  $\times$  2k UltraScan CCD camera (Gatan). TEM samples were precisely positioned inside of a cryo high-tilt TEM holder (Gatan 626) to ensure that the 9  $\times$  9 fiducial square stayed within an error of approximately 10 degrees parallel to the CCD camera edge. After finishing the first tilt series, the holder was briefly removed from the microscope and the sample manually rotated by 90 degrees. Un-binned images have a pixel size of 0.3819 nm corresponding to a magnification of 29 k $\times$  on the CCD camera. The sample region was exposed to a beam produced by the spot size of 1 and C2 aperture 2, with the intensity held constant during the tilt series. Brightfield image contrast was produced using objective aperture 2. A target of 500 nm under-focus was chosen to keep the sample volume on the same side of the image plane for all tilt angles and to omit contrast reversal of the interference contrast at gold particle and silica surfaces. 141 images were recorded for each tilt axis, covering a range from –70 to +70 degrees with constant increments at 1 degree. The tomography data were reconstructed using IMOD software<sup>[49]</sup> in which the tilt series were aligned using a cross-correlation algorithm and the fiducial markers for the rough and fine alignment, respectively. Both tilt series were reconstructed separately using a weighted back-projection algorithm and combined into one reconstruction. Further image processing and visualization were carried out in imageJ.<sup>[50]</sup>

**Quantification of Metal-Support Interface:** The quantification of the exposed and embedded particle surface was carried out using a Python custom code based on the scikit-image package.<sup>[51]</sup> Details are provided in the Supporting Information, along with Figures S3, S6–S8, Supporting Information.

**Additional Characterization Techniques:** The optical properties of the Au-core Ag-shell NPs were investigated with ultraviolet-visible spectroscopy (UV–vis). The spectra were recorded from 300–700 nm with a 0.5 nm step size, in an aqueous solution using a Beckman Coulter DU720 spectrometer. The composition and metal loading for the Au(Pd)@SiO<sub>2</sub> catalysts were determined using ICP-MS (Agilent Technologies 7700x). The porosity of the SiO<sub>2</sub> matrix was analyzed by nitrogen physisorption at –196 °C, using a 3Flex high resolution, high-throughput physisorption, and chemisorption instrument (Micromeritics). Prior to the physisorption measurement, the sample (100 mg SiO<sub>2</sub> RCT) was dried at 200 °C (+10 °C min<sup>-1</sup>) in N<sub>2</sub> for 12 h.

*Numerical Calculation of the Equilibrium State Interfacial Shapes:* To check the formation conditions and resultant areal portion of exposed gold NPs on the final RCT materials, a numerical calculation model was employed using the Surface Evolver program (a finite element method-based numerical calculation software, <http://facstaff.susqu.edu/brakke/evolver/evolver.html>).<sup>[52]</sup> The computer simulation model calculated the equilibrium state shape of the liquid-vapor interface that develops during the infiltration stage before the removal of PS colloid particle under user-specified initial conditions. In the model, it was assumed that both PS colloid and gold NP were rigid spheres and made a point contact, and that the three-phase contact line showed no contact angle hysteresis. With the small equilibrium contact angle of the fluid (i.e.,  $\approx 30^\circ$  and  $10^\circ$  of the silica sol-gel solution on the PS surface and gold surface, respectively), a finite volume of vapor was introduced to the model, and the geometry of the equilibrium contact lines was calculated for various air volumes trapped.

## Supporting Information

Supporting Information is available from the Wiley Online Library or from the author.

## Acknowledgements

This work was supported as part of the Integrated Mesoscale Architectures for Sustainable Catalysis (IMASC), an Energy Frontier Research Center funded by the U.S. Department of Energy, Office of Science, Basic Energy Sciences under Award # DE-SC0012573. The work was performed in part at the Center for Nanoscale Systems (CNS), a member of the National Nanotechnology Coordinated Infrastructure Network (NNCI), which was supported by the National Science Foundation under NSF ECCS award no. 1541959. The authors thank Dr. Michael Aizenberg for critically reading the manuscript.

## Conflict of Interest

The authors declare no conflict of interest.

## Author Contributions

J.A., C.M.F., and J.v.d.H. initiated the project. J.v.d.H. and T.S. synthesized the samples. S.K. acquired the TEM tomography data and provided the algebraic reconstructions, advised by D.B. The dual-axis reconstruction was provided by J.v.d.H. The quantitative analysis was developed by S.D., advised by C.H.R. K.K.P. performed the numerical calculations. J.v.d.H. developed the metal overgrowth methodology and wrote the manuscript together with J.A. and with contributions of all authors.

## Data Availability Statement

Research data are not shared.

## Keywords

catalyst design, chemical accessibility, epitaxial overgrowth, metal-support interfaces, sintering

Received: July 15, 2021  
Revised: August 16, 2021  
Published online:

- [1] A. T. Bell, *Science* **2003**, 299, 1688.
- [2] G. Prieto, J. Zečević, H. Friedrich, K. P. De Jong, P. E. De Jongh, *Nat. Mater.* **2013**, 12, 34.
- [3] L. Wang, L. Wang, X. Meng, F. S. Xiao, *Adv. Mater.* **2019**, 31, 1901905.
- [4] J. E. S. van der Hoeven, J. Jelic, L. A. Olthof, G. Totarella, R. J. A. van Dijk-Moes, F. Studt, A. van Blaaderen, P. E. de Jongh, *Nat. Mater.* **2021**, 20, 1216.
- [5] P. M. Arnal, M. Comotti, F. Schüth, *Angew. Chem., Int. Ed.* **2006**, 45, 8224.
- [6] J. Chen, R. Zhang, L. Han, B. Tu, D. Zhao, *Nano Res.* **2013**, 6, 871.
- [7] C. H. Lin, X. Liu, S. H. Wu, K. H. Liu, C. Y. Mou, *J. Phys. Chem. Lett.* **2011**, 2, 2984.
- [8] H. Tang, Y. Su, B. Zhang, A. F. Lee, M. A. Isaacs, K. Wilson, L. Li, Y. Ren, J. Huang, M. Haruta, B. Qiao, X. Liu, C. Jin, D. Su, J. Wang, T. Zhang, *Sci. Adv.* **2017**, 3, e1700231.
- [9] J. Zhang, L. Wang, B. Zhang, H. Zhao, U. Kolb, Y. Zhu, L. Liu, Y. Han, G. Wang, C. Wang, D. S. Su, B. C. Gates, F. S. Xiao, *Nat. Catal.* **2018**, 1, 540.
- [10] E. D. Goodman, J. A. Schwalbe, M. Cargnello, *ACS Catal.* **2017**, 7, 7156.
- [11] Y. Kang, X. Ye, J. Chen, L. Qi, R. E. Diaz, V. Doan-Nguyen, G. Xing, C. R. Kagan, J. Li, R. J. Gorte, E. A. Stach, C. B. Murray, *J. Am. Chem. Soc.* **2013**, 135, 1499.
- [12] M. T. Bore, H. N. Pham, T. L. Ward, A. K. Datye, *Chem. Commun.* **2004**, 2620.
- [13] J. Liu, Q. Ji, T. Imai, K. Ariga, H. Abe, *Sci. Rep.* **2017**, 7, 41773.
- [14] L. de Rogatis, M. Cargnello, V. Gombac, B. Lorenzut, T. Montini, P. Fornasiero, *ChemSusChem* **2010**, 3, 24.
- [15] J. C. Matsubu, S. Zhang, L. DeRita, N. S. Marinkovic, J. G. Chen, G. W. Graham, X. Pan, P. Christopher, *Nat. Chem.* **2017**, 9, 120.
- [16] E. Shirman, T. Shirman, A. V. Shneidman, A. Grinthal, K. R. Phillips, H. Whelan, E. Bulger, M. Abramovitch, J. Patil, R. Nevarez, J. Aizenberg, *Adv. Funct. Mater.* **2018**, 28, 1704559.
- [17] T. Shirman, J. Lattimer, M. Luneau, E. Shirman, C. Reece, M. Aizenberg, R. J. Madix, J. Aizenberg, C. M. Friend, *Chem. - Eur. J.* **2018**, 24, 1833.
- [18] T. Shirman, T. J. Toops, E. Shirman, A. V. Shneidman, S. Liu, K. Gurkin, J. Alvarenga, M. P. Lewandowski, M. Aizenberg, J. Aizenberg, *Catal. Today* **2021**, 360, 241.
- [19] M. Luneau, T. Shirman, A. Filie, J. Timoshenko, W. Chen, A. Trimpalis, M. Flytzani-Stephanopoulos, E. Kaxiras, A. I. Frenkel, J. Aizenberg, C. M. Friend, R. J. Madix, *Chem. Mater.* **2019**, 31, 5759.
- [20] M. Luneau, T. Shirman, A. C. Foucher, K. Duanmu, D. M. A. Verbart, P. Sautet, E. A. Stach, J. Aizenberg, R. J. Madix, C. M. Friend, *ACS Catal.* **2020**, 10, 441.
- [21] M. Luneau, E. Guan, W. Chen, A. C. Foucher, N. Marcella, T. Shirman, D. M. A. Verbart, J. Aizenberg, M. Aizenberg, E. A. Stach, R. J. Madix, A. I. Frenkel, C. M. Friend, *Commun. Chem.* **2020**, 3, 46.
- [22] A. Filie, T. Shirman, M. Aizenberg, J. Aizenberg, C. M. Friend, R. J. Madix, *Catal. Sci. Technol.* **2021**, 11, 4072.
- [23] J. E. S. van der Hoeven, H. T. Ngan, A. Taylor, N. M. Eagan, J. Aizenberg, P. Sautet, R. J. Madix, C. M. Friend, *ACS Catal.* **2021**, 11, 6971.
- [24] A. Filie, T. Shirman, A. C. Foucher, E. A. Stach, M. Aizenberg, J. Aizenberg, C. M. Friend, R. J. Madix, *J. Catal.* **2021**.
- [25] K. R. Phillips, T. Shirman, M. Aizenberg, G. T. England, N. Vogel, J. Aizenberg, *J. Mater. Chem. C* **2019**, 8, 109.
- [26] H. Wu, D. Wang, D. K. Schwartz, *J. Phys. Chem. Lett.* **2020**, 11, 8825.
- [27] M. Weyland, P. A. Midgley, J. M. Thomas, *J. Phys. Chem. B* **2001**, 105, 7882.
- [28] J. Zečević, K. P. De Jong, P. E. De Jongh, *Curr. Opin. Solid State Mater. Sci.* **2013**, 17, 115.
- [29] J. P. Tessonnier, O. Ersen, G. Weinberg, C. Pham-Huu, D. S. Su, R. Schlögl, *ACS Nano* **2009**, 3, 2081.

- [30] J. C. Hernández-Garrido, K. Yoshida, P. L. Gai, E. D. Boyes, C. H. Christensen, P. A. Midgley, *Catal. Today* **2011**, *160*, 165.
- [31] P. Penczek, M. Marko, K. Buttle, J. Frank, *Ultramicroscopy* **1995**, *60*, 393.
- [32] P. Ercius, O. Alaidi, M. J. Rames, G. Ren, *Adv. Mater.* **2015**, *27*, 5638.
- [33] I. Arslan, J. R. Tong, P. A. Midgley, *Ultramicroscopy* **2006**, *106*, 994.
- [34] H. Sugimori, T. Nishi, H. Jinnai, *Macromolecules* **2005**, *38*, 10226.
- [35] D. N. Mastronarde, *J. Struct. Biol.* **1997**, *120*, 343.
- [36] M. Liu, P. Guyot-Sionnest, *J. Phys. Chem. B* **2005**, *109*, 22192.
- [37] M. C. Scott, C. C. Chen, M. Mecklenburg, C. Zhu, R. Xu, P. Ercius, U. Dahmen, B. C. Regan, J. Miao, *Nature* **2012**, *483*, 444.
- [38] A. S. Barnard, N. P. Young, A. I. Kirkland, M. A. Van Huis, H. Xu, *ACS Nano* **2009**, *3*, 1431.
- [39] J. E. S. Van Der Hoeven, T. Deng, W. Albrecht, L. A. Olthof, M. A. Van Huis, P. E. De Jongh, A. Van Blaaderen, *ACS Omega* **2021**, *6*, 7034.
- [40] N. R. Jana, L. Gearheart, C. J. Murphy, *Chem. Commun.* **2001**, 617.
- [41] T. W. Hansen, A. T. Delariva, S. R. Challa, A. K. Datye, *Acc. Chem. Res.* **2013**, *46*, 1720.
- [42] N. Masoud, T. Partsch, K. P. de Jong, P. E. de Jongh, *Gold Bull.* **2019**, *52*, 105.
- [43] A. Surrey, D. Pohl, L. Schultz, B. Rellinghaus, *Nano Lett.* **2012**, *12*, 6071.
- [44] B. Dong, Y. Pei, F. Zhao, T. W. Goh, Z. Qi, C. Xiao, K. Chen, W. Huang, N. Fang, *Nat. Catal.* **2018**, *1*, 135.
- [45] S. H. Petrosko, R. Johnson, H. White, C. A. Mirkin, *J. Am. Chem. Soc.* **2016**, *138*, 7443.
- [46] K. D. Gilroy, A. Ruditskiy, H. C. Peng, D. Qin, Y. Xia, *Chem. Rev.* **2016**, *116*, 10414.
- [47] K. C. Grabar, K. J. Allison, B. E. Baker, R. M. Bright, K. R. Brown, R. G. Freeman, A. P. Fox, C. D. Keating, M. D. Musick, M. J. Natan, *Langmuir* **1996**, *12*, 2353.
- [48] J. Piella, N. G. Bastús, V. Puntès, *Chem. Mater.* **2016**, *28*, 1066.
- [49] J. R. Kremer, D. N. Mastronarde, J. R. McIntosh, *J. Struct. Biol.* **1996**, *116*, 71.
- [50] J. Schindelin, I. Arganda-Carreras, E. Frise, V. Kaynig, M. Longair, T. Pietzsch, S. Preibisch, C. Rueden, S. Saalfeld, B. Schmid, J. Y. Tinevez, D. J. White, V. Hartenstein, K. Eliceiri, P. Tomancak, A. Cardona, *Nat. Methods* **2012**, *9*, 676.
- [51] S. Van Der Walt, J. L. Schönberger, J. Nunez-Iglesias, F. Boulogne, J. D. Warner, N. Yager, E. Gouillart, T. Yu, *PeerJ* **2014**, *2014*, e453.
- [52] K. A. Brakke, *Exp. Math.* **1992**, *1*, 141.